Successive Ionic Layer Adsorption and Reaction-Deposited Transparent Cu–Zn–S Nanocomposites as Hole Transport Materials in CdTe Photovoltaics

Ebin Bastola, Kamala Khanal Subedi, Fadhil K. Alfadhili, Adam B. Phillips, Michael J. Heben, and Randy J. Ellingson

Evolving material science and device architectures continue to drive improvements in photovoltaic solar cell performance. Herein, the synthesis and application of p-type transparent copper–zinc–sulfide (Cu–Zn–S) nanocomposite thin films for application as a semi-transparent back buffer layer for cadmium telluride (CdTe) photovoltaics is reported. Earth-abundant and low-toxicity Cu–Zn–S films are prepared at room temperature using successive ionic layer adsorption and reaction (SILAR). Transparency in the range of 500–800 nm, low resistivity, and composition-controlled bandgap energy offer a compelling material system for high performance as an electron reflector enabling bifacial cell design. Implementing the Cu–Zn–S hole transport material (HTM) at the CdTe back contact, without intentional introduction of Cu doping, converts simulated AM1.5 sunlight to electricity at an efficiency up to 13.2%, with an average device performance of 13.0%. Intentional Cu doping yields a best efficiency of 14.3% with open-circuit voltage (V_{OC}) of 848 mV and fill factor (FF) of 77.3% (average 14.1%). Our study shows the clear promise of this material for highly efficient and semi-transparent back contact to CdTe solar cells.

1. Introduction

Transparent conducting materials are essential to fabricate electronic devices such as light-emitting diodes,[1] displays,[2] and photovoltaic devices.[3] The thin-film solar cell device consists of transparent conducting materials as a window and/or buffer layer and a semiconductor material as an absorber layer. The transparent materials possess both high conductivity (low resistivity) and optical transparency which are, in general, n-type materials. However, the buffer layers or hole transport materials (HTMs), which are applied at the back-contact interface, such as in cadmium telluride (CdTe) solar cells, are p-type.

Dr. E. Bastola, K. K. Subedi, Dr. F. K. Alfadhili, Prof. A. B. Phillips, Prof. M. J. Heben, Prof. R. J. Ellingson
Wright Center for Photovoltaics Innovation and Commercialization (PVIC)
Department of Physics and Astronomy
University of Toledo
Toledo, OH 43606, USA
E-mail: Randy.Ellingson@utoledo.edu

The ORCID identification number(s) for the author(s) of this article can be found under https://doi.org/10.1002/ente.202000429.

The development of p-type transparent materials with high hole conductivity and optical transparency lags behind compared with n-type transparent materials.[4] Common p-type transparent conducting materials, also important for the fabrication of bifacial photovoltaic devices, include oxide and sulfide compounds of copper such as Cu_xO,[5] $CuAlO_2$,[6] Cu_xS,[7] and $Cu_xZn_{1-x}S$.[8]

Cu–Zn–S (CZS) nanocomposite thin films are Earth-abundant materials possessing high transparency in the visible region, a high energy bandgap, high conductivity, and high hole concentration.[9] The optical bandgap and Fermi level of the CZS material can be adjusted by changing the material composition.[10] Thus, CZS nanocomposite can serve as effective hole selective layers in solar cells.[3a] CZS materials can be prepared by vacuum[11] and solution-based techniques including chemical bath deposition (CBD)[3a,12] and successive ionic layer adsorption and reaction (SILAR)[9,10] methods. Xu et al. have reported $(CuS)_x(ZnS)_{1-x}$ p-type transparent materials with transmission >70% in the visible region and fabricated heterojunction p-$(CuS)_x(ZnS)_{1-x}$/n-Si solar cells.[3a] The $(CuS)_x(ZnS)_{1-x}$ nanocomposites served as the hole selective layers for heterojunction devices and demonstrated the application of these Earth-abundant materials as HTMs in solar cells. Previously, we have fabricated CdTe devices with $(CuS)_x(ZnS)_{1-x}$ as the hole selective layer using CBD.[13] Jose et al. have synthesized and characterized the CZS film using a SILAR method.[9] In a SILAR method, the material gets deposited by the reactions of cations and anions, producing an atomic layer and thus improving the quality of the nanocomposite films. In addition, the thin films with very small grain sizes are more compact and transparent to visible light.

Cadmium telluride (CdTe) solar cells are well-known thin-film technologies that convert solar energy into electrical energy with a suitable bandgap of 1.48 eV. To fabricate CdTe solar cells, copper/gold (Cu/Au) is usually used as a standard back-contact material, and the role of Cu is for doping and band bending due to a deeply located ($\approx$−5.9 eV)[14] valence band edge of CdTe.[15] The work function of gold is $\approx$5.0–5.2 eV[16] compared with the deep valence band edge of CdTe, a potential barrier is formed.

**ADVANCED
SCIENCE NEWS**
www.advancedsciencenews.com

Energy Technology
Generation, Conversion, Storage, Distribution
www.entechnol.de

To reduce this potential barrier, one utilizes a material with suitable optoelectronic properties (p-type, low resistivity, high hole concentration) and band edge location to achieve efficient extraction of holes while repelling electrons at the back interface of the CdTe devices; the desired results include a reduced forward electron current and improved open-circuit voltage.[17] Materials such as carbon nanotubes,[18] copper thiocyanate (CuSCN),[19] iron pyrite (FeS$_2$),[20] zinc telluride (ZnTe),[21] antimony telluride (Sb$_2$Te$_3$),[22] and copper telluride (Cu$_x$Te)[23] have been tested as back-contact buffer layers in CdTe solar cells. First solar has used ZnTe as an interface layer to fabricate highly efficient CdTe solar cells on a commercial scale.[24] Some of the solution-processed back-contact buffer layers include Ni$_x$Fe$_{1-x}$S$_2$, chalcopyrite (CuFeS$_2$), and perovskite.[25] Similarly, some of the materials used as hole transport layers in nanocrystal-based CdTe solar cells include P-TPA, Si-TPA, and Spiro to improve the hole transport properties and device efficiency.[26] However, most of these materials are not optically transparent to visible light for the fabrication of bifacial devices, and their doping level cannot be well controlled. We demonstrate that Earth-abundant materials such as Cu–Zn–S can be alternatives HTMs in photovoltaics.

Previously, we have fabricated (CuS)$_x$(ZnS)$_{1-x}$ thin films using a CBD method at 80 °C in about an hour and applied them as HTMs for CdTe photovoltaics.[13] During deposition, Cu ions may diffuse to the CdTe film and we were interested to see how room temperature-processed CZS acts as HTMs to CdTe photovoltaics, assuming that there is no Cu diffusion at room temperature. Our preliminary study of CZS HTMs deposited by the SILAR method on CdTe showed a promising result without additional Cu doping and inspired us to carry this investigation over a wide range of CZS compositions.[27] Here, we have fabricated and characterized transparent CZS nanocomposite thin films with various compositions, using a SILAR method, and then applied them as a back-contact interface layer to CdTe solar cells. These CZS films are compact with petal-like nanostructures with high transparency in the visible region and low resistivity with varying bandgap energy. We found that CdTe devices with a CZS layer performed better compared with the devices without the CZS layer, reaching an efficiency of 13.2%. With optimized doping and CZS nanocomposite as an interface layer, the best cell reached an efficiency of 14.3% (average 14.1%) with an open-circuit voltage of 848 mV and a fill factor (FF) of 77.3%.

2. Results and Discussion

The CZS thin films were fabricated at room temperature using a SILAR method. In the first step, cations were adsorbed on the surface, and weakly bound cations were removed during subsequent rinsing in DIW. The substrate is then immersed in anion solution, resulting a reaction between cations (Zn and Cu ions) and anions (S ions), followed by additional rinse in DIW which removes loosely bound S ions. The SILAR cycle is repeated several times to prepare a thin film of desired thickness. **Figure 1** shows the transmission and reflection spectra for CZS-10, CZS-20, CZS-30, CZS-40, CZS-50, and CZS-80 nanocomposite films. Here, CZS-30 denotes thin films prepared using Zn precursor
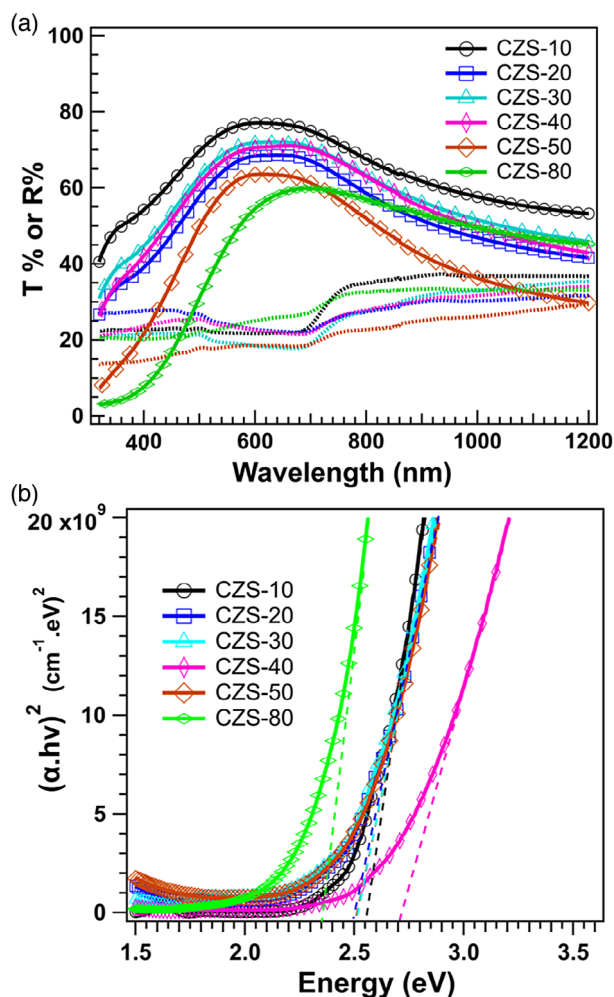
Figure 1. a) Transmission (T) and reflection (R, dotted) spectra of the CZS nanocomposite thin films prepared by a SILAR method and b) plots of $(\alpha h\nu)^2$ versus energy ($h\nu$, eV) to estimate the energy bandgaps of CZS nanocomposites (CZS-30 represents a film prepared using 0.03 M zinc acetate and 0.07 M CuCl$_2$ as cationic precursor).

30% (0.03 M zinc acetate) and Cu precursor 70% (0.07 M) of the total cations (0.1 M) used. As shown in the transmission spectra, these films show greater than 50% transmittance in the visible region in the range of 500–800 nm. The transmission and reflection spectra were utilized to obtain bandgaps of these films. The transmission (T) and reflection (R) spectra along with the thickness (t) of the films were used to calculate the absorption coefficient (α) of the thin film using the equation

$$\alpha = -\ln(T/(1-R))/t \tag{1}$$

The bandgap energies for these nanocomposites were calculated by plotting $(\alpha h\nu)^2$ versus $(h\nu)$ for CZS nanocomposites. The calculated bandgap values for CZS films are shown in **Table 1**. The energy bandgap of the CZS-30 film estimated by the equation earlier is 2.50 eV.

Figure 2 shows the surface morphology of CZS thin films deposited on a soda lime glass for CZS-10, CZS-30,

Table 1. Properties of Cu–Zn–S thin films.

Sample	Thickness [nm]	$T\%$ at 550 [nm]	Bandgap (E_g, [eV])	Sheet resistance [Ω sq^{-1}]	Resistivity (10^{-2} [Ω cm])
CZS-10	50	75.2	2.55	3143	1.6
CZS-20	100	65.3	2.50	1322	1.3
CZS-30	90	69.5	2.50	2166	2.0
CZS-40	145	67.9	2.70	6102	8.9
CZS-50	180	60.0	2.50	2918	5.3
CZS-80	200	45.1	2.35	38 956	77.9

CZS-50, and CZS-80. Based on scanning electron microscopy (SEM) images, CZS-30 and CZS-50 films have similar surface morphologies with compact grains of length of around 200 nm. CZS-10 film was thinner ($\approx$50 nm) compared with other films, has higher transparency, and consists of voids compared with CZS-30 and CZS-50 films. Note that all these films were deposited in the same condition and only the ratio of cations (Zn and Cu ions) were varied. In the case of CZS-80 film (Figure 2d), surface morphology looks different from other CZS compositions which might be due to a higher amount of Zn atoms in the cationic precursor. CZS-50 film had few diffraction peaks[27] similar to CuS, whereas CZS-80 film shows an amorphous nature compared with other compositions (Figure S1, Supporting Information). Energy-dispersive X-ray spectroscopy (EDS) analysis of these films shows elemental composition consisting of Cu, Zn, and S atoms and the atomic percentages of constituent elements are shown in Table S1, Supporting Information. No Zn atoms were observed in the EDS analysis for CZS-10 and CZS-20 films. The Zn percentage was increased to higher amounts as the amount of Zn percentage was increased in the precursor. Here, the lower content of Zn in the film compared with the precursor indicates the lower

reactivity of Zn atoms compared with Cu atoms, as observed in $(CuS)_x(ZnS)_{1-x}$ deposition using the chemical bath method.[13]

Based on X-ray diffraction patterns (Figure S1, Supporting Information), as-deposited CZS thin films with higher Cu (lower Zn) concentrations have diffraction patterns similar to the covellite CuS (hexagonal crystal structure) but with lower Cu (higher Zn) concentrations, no diffraction patterns were observed. It indicates poor crystallinity as the Zn atoms increase, which is slightly different with the previous report.[9] The authors observed diffraction patterns for various compositions of CZS films. CZS-20 film shows a small diffraction peak at 48.2°, matching a peak of CuS (PDF #98-001-3414). In the case of CZS-50 sample, its diffraction peaks match well with the standard covellite CuS peaks. However, no diffraction peaks were observed for CZS-80 film, indicating the amorphous nature of the materials deposited, similar to the CBD-deposited $(CuS)_x(ZnS)_{1-x}$ film. As the amount of Zn in the film increases the film becomes more amorphous.[3a,13]

The sheet resistances of CZS films were measured using a four-point probe and resistivities were calculated. Table 1 shows the various properties of these nanocomposite films including thickness, transmission at 550 nm wavelength, energy bandgap, sheet resistance, and resistivity. As the amount of Zn concentration increased, its resistivity increased. For example, for CZS-10, the resistivity is 1.6×10^{-2} Ω cm whereas for CZS-80, the resistivity is 77.9×10^{-2} Ω cm. The resistivity increases due to the lower amount of Cu content and the more amorphous nature of the nanocomposite film. The resistivities measured for these CZS films are similar to the values reported previously and these materials have hole concentrations in the order of 10^{21} cm^{-3}, thus behaving like degenerately doped semiconductors.[9] The transparency of these nanocomposite films in the visible region and low resistivity make these materials promising in various optoelectronic applications including light-emitting devices, displays, and solar cells. As evidenced from the low resistivity
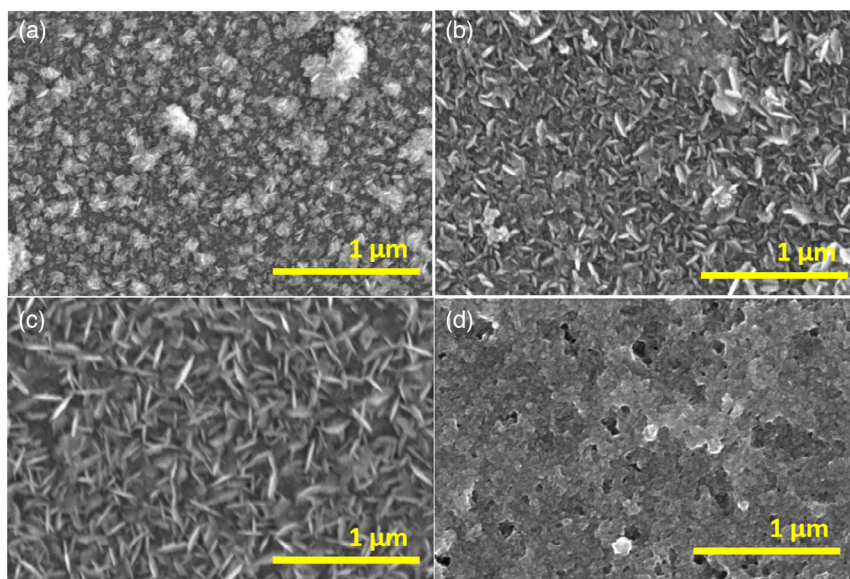
Figure 2. SEM images of Cu–Zn–S thin films: a) CZS-10, b) CZS-30, c) CZS-50, and d) CZS-80 (CZS-30 represents a film prepared using 0.03 M zinc acetate and 0.07 M CuCl₂ as cationic precursor).

(high conductivity) of these CZS films, high hole concentration, and the change of its Fermi level with composition, these materials can be good contact materials for solar cells.[3a]

To study the hole transport properties, CZS thin films were deposited on CdTe devices and covered with 40 nm Au to complete the back contact. **Figure 3** shows a schematic and a cross-sectional image of the CdTe device with a CZS layer as the hole transport layer. These devices were completed after the deposition of the CZS film at room temperature and without any thermal annealing. The $J–V$ characteristics for the best cells of the controlled device and with CZS as HTMs under light and dark measurement conditions are shown in **Figure 4**a and the quantum efficiency measurements are shown in Figure S2, Supporting Information. The best cell has an efficiency of 10.5% for Au only back contact with an average device performance of 10.0% for 20 cells and the best back contact was CZS-30/Au with an average device performance of 12.8%, with the best cell performance of 13.1%. The CZS-30/Au back contact best cell has a higher V_{OC} of 816 mV and FF of 74.4%. Based on the literature, Jose et al. reported that the CZS-30 film deposited by a SILAR method has the highest hole density of 1.01×10^{22} cm^{-3} compared with other CZS nanocomposites and a mobility of 2.68 cm^2 V^{-1} S^{-1}.[9] Thus, due to the

Figure 3. Schematic device diagram and cross-sectional SEM image of CdTe solar cells with Cu–Zn–S (CZS-50) as a back-contact interface layer.

Figure 4. $J–V$ characteristics of CdTe photovoltaics with and w/o Cu–Zn–S (CZS) nanocomposites as HTMs.

higher doping level and hole mobility, CZS-30 back buffer layer performed better compared with other CZS nanocomposites.

The device performance for CZS-30/Au film is slightly higher than that of the controlled device with Cu/Au (3/40 nm) deposited by thermal evaporation (Table S2, Supporting Information). Note that in the case of devices with CZS films, no additional Cu layer was deposited. For CZS-80/Au back contact, the device efficiency was 3.9% with a significant drop in the FF (31.5%) and J_{SC} (15.2 mA cm^{-2}). The higher resistivity (Table 1) of the CZS-80 film than CZS-30 and CZS-50 films reduced the device performance, which is attributed to lower Cu/Zn ratio. Table S2, Supporting Information, shows average device parameters of the CdTe devices with various CZS nanocomposites and standard Cu/Au back contact. Due to the significant increase in the resistivity of the CZS-80 layer, we observed a significant increase in the series resiatnce (R_S) and drop in shunt resistance (R_{SH}) of the device with CZS-80 layer, which finally reduced the device performance. Previously, CZS layer deposited by CBD at 80 °C was also used as HTMs in CdTe devices and the champion cell efficiency was 13.0% (V_{OC} 805 mV, J_{SC} 22.1 mA cm^{-2}, and FF 73.3%) with CZS layer and Cu/Au (3/40 nm) back contact.[13] During thermal annealing after Cu evaporation, there was a loss in the FF than the standard Cu/Au device which might be due to the over heat treatment. Here, for room temperature-deposited CZS-30/Au back contact, the device efficiency is similar without an additional evaporated Cu layer and thermal annealing (Figure 4), which indicate that efficient devices can be fabricated by depositing a CZS nanocomposite at room temperature. To see the effect of annealing after the deposition of CZS layer on CdTe devices, we annealed the devices at 200 °C for 10 min and measured after annealing. The device performance was poor compared with the unannealed device as the loss of V_{OC}, J_{SC}, and FF occurs (Figure S3, Supporting Information). Based on this observation, we conclude that during thermal annealing, weakly bounded Cu, Zn, and S atoms from the CZS layer diffuse into CdTe film, lowering the device characteristics.

Further, we analyzed the surface morphology of CdTe films with CZS layer on top with electron microscopy, X-ray diffraction, and EDS analysis. CZS nanocomposites can be observed on the top surface of CdTe, indicating the change in surface morphology, as shown in **Figure 5**a,b. The shapes of CZS particles on the CdTe surface look slightly different from the CZS nanocomposite formed on a soda lime glass substrate. However, the elemental composition revealed Cu, Zn, and S atoms in addition to Cd, Te, and Cl atoms. Note that these CZS films were deposited after CdCl$_2$ treatment on CdTe devices. EDS analysis for standard CdTe and with a CZS layer is shown in Table S3, Supporting Information. The X-ray diffraction (XRD) pattern of the CdTe film with CZS layer reveals small diffraction peaks of CuS with other strong diffraction peaks of CdTe, as shown in Figure 5c. The peak marked by * is usually observed on CdTe surface after CdCl$_2$ treatment, which may be due to the formation of CdTeO$_x$ present on the surface.[28] The XRD pattern was compared with standard powder diffraction files (PDF) of CdTe (PDF # 97-005-2840) and CuS (PDF #98-001-3414) on the MDI ZADE software.

Here, we also investigated CdTe devices with CZS-30 layer of various thicknesses (deposition cycles) and additional Cu-doped CdTe devices with CuCl$_2$ treatment. Previously, we have reported
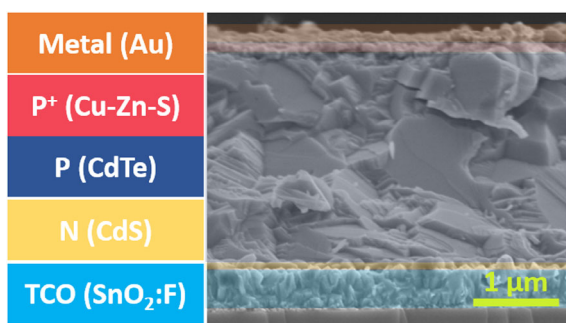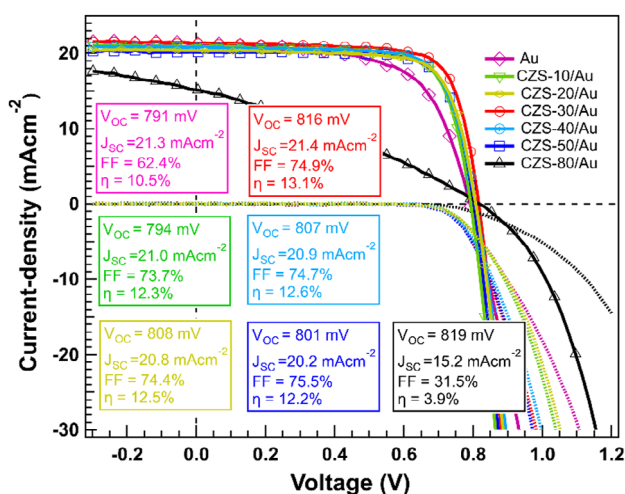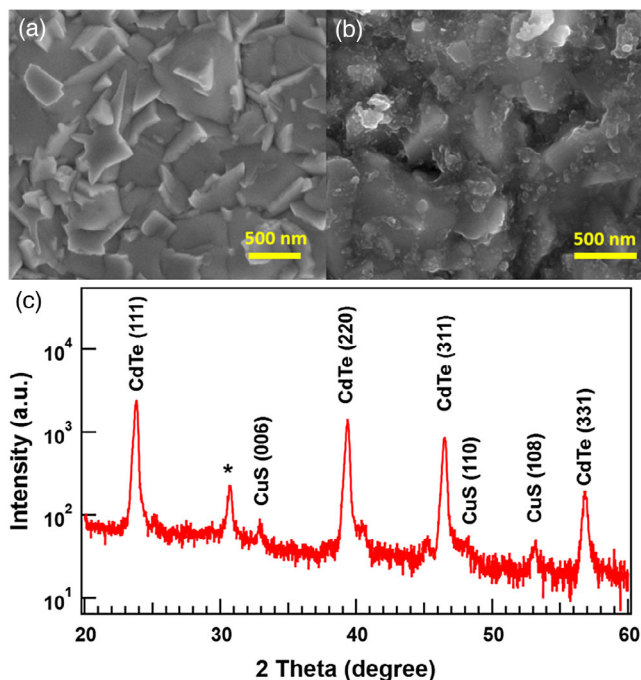
Figure 5. SEM images of CdTe surface a) without CZS nanocomposites, b) with CZS nanocomposites, and c) X-ray diffraction pattern of CdTe film with CZS-30 nanocomposites. The standard diffraction patterns for CdTe and CuS are PDF #97-005-2840 and PDF #98-001-3414, respectively.

that highly efficient CdTe devices can be fabricated than evaporated Cu by doping with $CuCl_2$ solution and device performance increases mainly due to the improvement in V_{OC} and FF.[29] CdTe devices with different thicknesses/deposition cycles of CZS-30 nanocomposites were fabricated and measured under the standard AM1.5G solar spectrum. The average device performance is shown in **Figure 6**a for various deposition cycles from 0 to 60 and J–V characteristics of the best cells are shown in Figure 6b for CZS-30 nanocomposites with 0, 5, 10, 20, 40, and 60 deposition cycles. Based on these J–V characteristics, we found that CZS-30 with ten deposition cycles performed the best compared with other deposition cycles. The average device efficiency is 13.0% with the best cell having an efficiency of 13.2% with V_{OC} of 834 mV, J_{SC} of 21.6 mA cm^{-2}, and FF of 72.9%. We attribute the higher device efficiency, especially V_{OC}, to the better band alignment of CdTe with CZS nanocomposite.[17] The average device parameters are shown in Table S4, Supporting Information. The average efficiency of the device with a higher number of deposition cycles was lower than ten deposition cycles mainly due to the loss in FF, which is due to the increase in series resistance of the device (a thicker CZS composite on the back of the device).

Further, we tested the effect of these CZS layers on top of CdTe devices after copper chloride ($CuCl_2$) treatment. For this, CdTe devices after $CdCl_2$ treatment were submerged in 0.1 mmol $CuCl_2$ solution in deionized water (DIW) and annealed at 200 °C for 20 mins.[29,30] After this, CZS-30 layer with 10 deposition cycles was deposited on one of the devices and J–V measurement was carried out. Figure 6c shows the J–V characteristics of the best cells of the control and CZS deposited device.
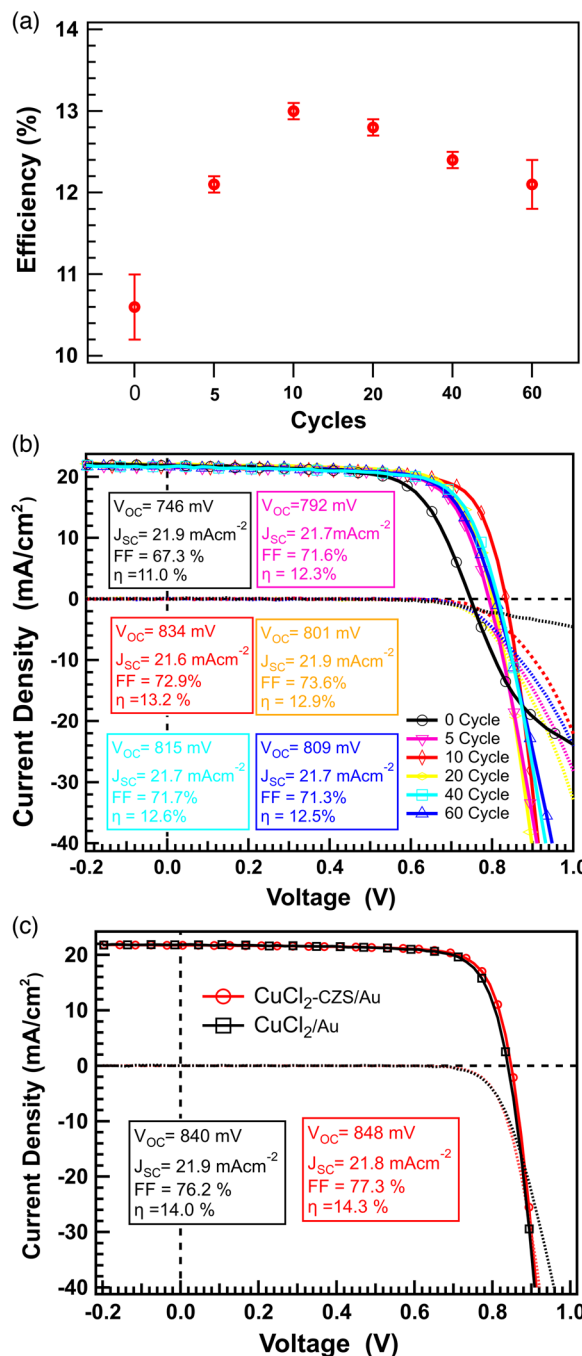
Figure 6. Device characteristics of CdTe solar cells with a) average device efficiency of CdTe cells, b) J–V characteristics of the best cells with various deposition cycles of CZS-30 nanocomposites, and c) J–V characteristics of the best cells for $CuCl_2$-treated CdTe device with CZS nanocomposite (average shown in Table 2).

The average device efficiency with $CuCl_2$/Au is 13.7% with the best cell reaching 14.0%, whereas $CuCl_2$/CZS/Au back contact shows an average device performance of 14.1%. The average device parameters are shown in **Table 2**. Using the CZS layer, the average increase in PCE is 2.9% whereas the FF was improved by 2.5% for 20 cells. The best cell with

Table 2. Average device parameters of 20 cells with and without CZS nanocomposite for CuCl$_2$-treated CdTe devices.

Back contact	V_{OC} [mV]	J_{SC} [mA cm^{-2}]	FF [%]	Eff. [η%]	R_s [Ω cm^2]	R_{sh} [Ω cm^2]
CuCl$_2$/Au	840 ± 2	21.6 ± 0.3	75.6 ± 0.4	13.7 ± 0.2	4.4 ± 0.1	2717 ± 227
CuCl$_2$/CZS/Au	845 ± 3	21.5 ± 0.2	77.4 ± 0.3	14.1 ± 0.1	2.8 ± 1.1	3100 ± 293

CuCl$_2$/CZS/Au has V_{OC} of 848 mV, J_{SC} of 21.8%, and FF of 77.3% with PCE of 14.3%. This efficiency is equivalent to 17.0% if other window layers (CdS:O, CdSe or MZO) were used to have J_{SC} of 26 mA cm^{-2}.[31] Due to the CZS nanocomposite layer, the device efficiency was enhanced mainly due to the improvement of FF of the device. The better device efficiency on using CZS nanocomposite is due to a reduced back barrier height and flattening of the conduction band compared with Au only or Cu/Au back contact.[27] The J–V–T measurement of CdTe devices with CZS-50 nanocomposite showed a back barrier height of 0.238 eV in between CZS-50/Au which is less compared with Au only (0.395 eV) and Cu/Au (0.330 eV) back contact.[27,32] This indicates that the CZS layer on the back of CdTe devices lowers the back barrier height, increasing the device efficiency.

3. Conclusions

Here, we have successfully fabricated Cu–Zn–S nanocomposite thin films at room temperature using the SILAR method which are transparent to visible light and have low resistivity. Further, room-temperature-processed transparent CZS films as the back-contact HTM in CdTe devices have been demonstrated. Out of the various compositions of nanocomposites, CZS-30/Au as the back contact has the highest efficiency 13.2% with no additional Cu. The CZS-80 film performed poorly (3.9%) due to its high resistivity and poor crystallinity. Similarly, for CuCl$_2$-treated CdTe devices with the CZS interface layer, the highest efficiency observed is 14.3% with an average device performance of 14.1%. Based on this study, CZS nanocomposite can be considered as a low-barrier interface layer to fabricate highly efficient devices, and other vacuum-based approaches can be sought for deposition of these CZS films.

4. Experimental Section

Materials: Copper (II) chloride (CuCl$_2$, 99.99%), zinc acetate (Zn (acac)$_2$, 99.9%), sodium sulfide (Na$_2$S.9H$_2$O, 98.0%), and triethanolamine (TEA) (≥99.0%) were obtained from Sigma Aldrich. Cadmium chloride (CdCl$_2$, ultradry, 99.996%) and methanol (CH$_3$OH, 98%) were obtained from Alfa Aesar. All the chemicals were used as obtained without further purification.

Cu–Zn–S Thin-Film Preparation: The CZS nanocomposite films were deposited at room temperature using a SILAR method, adapting a procedure from literature.[9,27] First, CZS thin films were deposited on a soda lime glass (SLG) substrate for characterization. For this, Micro-90 detergent was used to clean soda lime glasses by sonication for 30 min, followed by rinsing several times with DIW. Then, glasses were again cleaned using a sonicator in acetone, methanol, and 2-propanol for 5 min each.

CZS-30 film was deposited by preparing the cationic precursor by dissolving 0.07 M CuCl$_2$, 0.03 M zinc acetate in DIW, with a total concentration of 0.1 M, 5 mL TEA, keeping the total volume to 25 mL, and anionic precursor using 0.05 M Na$_2$S in DIW. Here, CZS-30 denotes thin films prepared using Zn precursor 30% (0.03 M zinc acetate) and Cu precursor

70% (0.07 M) of the total cations (0.1 M) used. The SLG substrate was placed in a cationic precursor for 15 s, rinsed in DIW for 5 s, in anionic precursor for 15 s, and in DIW for 5 s to complete one SILAR cycle. A dip coater from NIMA Technology was used to complete all the SILAR cycles. The same procedure was repeated to deposit CZS films on the CdTe film. Similarly, for CZS-40 film (40% zinc acetate in the cationic precursor), 0.04 M zinc acetate and 0.06 M CuCl$_2$ were used as the cationic precursor, keeping other chemicals same as CZS-30 film.

Device Fabrication: The CdS/CdTe device stacks received from Willard and Kelsey Solar Group were utilized for this study. Standard CdTe devices were completed using Cu/Au (3/40 nm) by thermal evaporation after CdCl$_2$ treatment in dry air environment. It was followed by thermal annealing of devices at 150 °C for about 35 min. To fabricate CZS as HTMs, CdCl$_2$-treated CdTe devices were used and CZS films were deposited using a SILAR method as mentioned earlier. Then, the devices were completed by depositing 40 nm Au. Similarly, for solution-based Cu doping, the CdTe film stack was submerged in 0.1 mmol CuCl$_2$ solution in DIW for 2 min, rinsed with DIW, and annealed at 200 °C for 20 mins.[29]

Film and Device Characterization: Hitachi S-4800 SEM, EDS, and PerkinElmer Lambda 1050 UV–Vis–NIR spectrophotometer were used to characterize the CZS thin films on soda lime glass. Rigaku Ultima III X-ray diffractometer operated at 40 KV, and 44 mA was used to obtain X-ray diffraction patterns. The four-point and Dektak profilometers were used to measure the sheet resistance and thickness, respectively. The completed devices were measured under simulated AM1.5G solar irradiance to find the photoconversion efficiency.

Supporting Information

Supporting Information is available from the Wiley Online Library or from the author.

Conflict of Interest

The authors declare no conflict of interest.

[1] H. Liu, V. Avrutin, N. Izyumskaya, Ü. Özgür, H. Morkoç, *Superlattices Microstruct.* **2010**, *48*, 458.

[2] E. Fortunato, P. Barquinha, R. Martins, *Adv. Mater.* **2012**, *24*, 2945.

[3] a) X. Xu, J. Bullock, L. T. Schelhas, E. Z. Stutz, J. J. Fonseca, M. Hettick, V. L. Pool, K. F. Tai, M. F. Toney, X. Fang, A. Javey, L. H. Wong, J. W. Ager, *Nano Lett* **2016**, *16*, 1925; b) W. Beyer, J. Hüpkes, H. Stiebig, *Thin Solid Films* **2007**, *516*, 147.

[4] G. Hautier, A. Miglio, G. Ceder, G. M. Rignanese, X. Gonze, *Nat. Commun.* **2013**, *4*, 2292.

[5] A. Parretta, M. Jayaraj, A. Di Nocera, S. Loreti, L. Quercia, A. Agati, *Phys. Status Solidi (a)* **1996**, *155*, 399.

[6] H. Kawazoe, M. Yasukawa, H. Hyodo, M. Kurita, H. Yanagi, H. Hosono, *Nature* **1997**, *389*, 939.

[7] M.-J. Zhang, Q. Lin, X. Yang, Z. Mei, J. Liang, Y. Lin, F. Pan, *Nano Lett.* **2016**, *16*, 1218.

[8] A. M. Diamond, L. Corbellini, K. Balasubramaniam, S. Chen, S. Wang, T. S. Matthews, L. W. Wang, R. Ramesh, J. W. Ager, *Phys. Status Solidi (a)* **2012**, *209*, 2101.

[9] E. Jose, M. C. Santhosh Kumar, *J. Alloys Compd.* **2017**, *712*, 649.

[10] M. A. Yıldırım, *Opt. Commun.* **2012**, *285*, 1215.

[11] S. K. Maurya, Y. Liu, X. Xu, R. Woods-Robinson, C. Das, J. W. Ager III, K. Balasubramaniam, *J. Phys. D: Appl. Phys.* **2017**, *50*, 505107.

[12] A. Mallick, S. Chattopadhyay, G. De, D. Basak, *J. Alloys Compd.* **2019**, *770*, 813.

[13] K. K. Subedi, E. Bastola, I. Subedi, Z. Song, K. P. Bhandari, A. B. Phillips, N. J. Podraza, M. J. Heben, R. J. Ellingson, *Sol. Energy Mater. Sol. Cells* **2018**, *186*, 227.

[14] J. L. Freeouf, J. M. Woodall, *Appl. Phys. Lett.* **1981**, *39*, 727.

[15] a) E. Janik, R. Triboulet, *J. Phys. D: Appl. Phys.* **1983**, *16*, 2333; b) E. Artegiani, J. D. Major, H. Shiel, V. Dhanak, C. Ferrari, A. Romeo, *Sol. Energy Mater. Sol. Cells* **2020**, *204*, 110228.

[16] B. de Boer, A. Hadipour, M. M. Mandoc, T. van Woudenbergh, P. W. M. Blom, *Adv. Mater.* **2005**, *17*, 621.

[17] G. K. Liyanage, A. B. Phillips, F. K. Alfadhili, R. J. Ellingson, M. J. Heben, *ACS Appl. Energy Mater.* **2019**, *2*, 5419.

[18] A. B. Phillips, R. R. Khanal, Z. Song, R. M. Zartman, J. L. DeWitt, J. M. Stone, P. J. Roland, V. V. Plotnikov, C. W. Carter, J. M. Stayancho, R. J. Ellingson, A. D. Compaan, M. J. Heben, *Nano Lett.* **2013**, *13*, 5224.

[19] A. Montgomery, L. Guo, C. Grice, R. A. Awni, S. Saurav, L. Li, Y. Yan, F. Yan, *Prog. Photovoltaics: Res. Appl.* **2019**, *27*, 665.

[20] K. P. Bhandari, P. Koirala, N. R. Paudel, R. R. Khanal, A. B. Phillips, Y. F. Yan, R. W. Collins, M. J. Heben, R. J. Ellingson, *Sol. Energy Mater. Sol. Cells* **2015**, *140*, 108.

[21] J. Li, D. R. Diercks, T. R. Ohno, C. W. Warren, M. C. Lonergan, J. D. Beach, C. A. Wolden, *Sol. Energy Mater. Sol. Cells* **2015**, *133*, 208.

[22] B. Siepchen, B. Späth, C. Drost, V. Krishnakumar, C. Kraft, M. Winkler, J. König, K. Bartholomé, S. Peng, *J. Electron. Mater.* **2015**, *44*, 3354.

[23] X. Wu, J. Zhou, A. Duda, Y. Yan, G. Teeter, S. Asher, W. K. Metzger, S. Demtsu, S.-H. Wei, R. Noufi, *Thin Solid Films* **2007**, *515*, 5798.

[24] N. Strevel, L. Trippel, C. Kotarba, I. Khan, *Photovoltaics Int.* **2013**, *22*, 66.

[25] a) E. Bastola, K. P. Bhandari, R. J. Ellingson, *J. Mater. Chem. C* **2017**, *5*, 4996; b) E. Bastola, K. K. Subedi, K. P. Bhandari, R. J. Ellingson, *MRS Adv.* **2018**, *3*, 2441; c) E. Bastola, K. P. Bhandari, I. Subedi, N. J. Podraza, R. J. Ellingson, *MRS Commun.* **2018**, *8*, 970; d) K. P. Bhandari, F. K. Alfadhili, E. Bastola, S. C. Watthage, Z. Song, G. K. Liyanage, A. J. Phillips, M. J. Heben, R. J. Ellingson, *Prog. Photovoltaics: Res. Appl.*, https://doi.org/10.1002/pip.3309.

[26] a) Z. Rong, X. Guo, S. Lian, S. Liu, D. Qin, Y. Mo, W. Xu, H. Wu, H. Zhao, L. Hou, *Adv. Funct. Mater.* **2019**, *29*, 1904018; b) X. Guo, Q. Tan, S. Liu, D. Qin, Y. Mo, L. Hou, A. Liu, H. Wu, Y. Ma, *Nano Energy* **2018**, *46*, 150; c) X. Du, Z. Chen, F. Liu, Q. Zeng, G. Jin, F. Li, D. Yao, B. Yang, *ACS Appl. Mater. Interfaces* **2016**, *8*, 900.

[27] E. Bastola, K. K. Subedi, F. K. Alfadhili, A. B. Phillips, M. J. Heben, R. J. Ellingson, in *IEEE 46th Photovoltaic Specialists Conf.*, IEEE, Chicago, IL **2019**, pp. 0144-0148.

[28] a) R. A. Awni, D.-B. Li, C. R. Grice, Z. Song, M. A. Razooqi, A. B. Phillips, S. S. Bista, P. J. Roland, F. K. Alfadhili, R. J. Ellingson, M. J. Heben, J. V. Li, Y. Yan, *Sol. RRL* **2019**, *3*, 1800304; b) E. Bastola, F. K. Alfadhili, A. B. Phillips, M. J. Heben, R. J. Ellingson, *J. Mater. Res.* **2019**, *34*, 3988.

[29] E. Bastola, A. V. Bordovalos, E. LeBlanc, N. Shrestha, M. O. Reese, R. J. Ellingson, *IEEE 46th Photovoltaic Specialists Conf.*, IEEE, Chicago, IL **2019**, pp. 1846–1850.

[30] D. Mao, G. Blatz, C. E. Wickersham, M. Gloeckler, *Sol. Energy Mater. Sol. Cells* **2016**, *157*, 65.

[31] a) D. E. Swanson, J. R. Sites, W. S. Sampath, *Sol. Energy Mater. Sol. Cells* **2017**, *159*, 389; b) X. Guo, Z. Rong, L. Wang, S. Liu, Z. Liu, K. Luo, B. Chen, D. Qin, Y. Ma, H. Wu, L. Hou, *Sustainable Energy Fuels* **2020**, *4*, 399.

[32] F. K. Alfadhili, A. B. Phillips, G. K. Liyanage, J. M. Gibbs, M. K. Jamarkattel, M. J. Heben, *MRS Adv.* **2019**, *4*, 913.